PHYSICAL REVIEW B **88**, 045136 (2013)

Effects of native defects on the structural and magnetic properties of hematite α-Fe_2O_3

Carlos Eduardo Cava,[1,2] Lucimara Stolz Roman,[2,3] and Clas Persson[1,4]
[1]*Department of Materials Science and Engineering, Royal Institute of Technology SE-100 44 Stockholm, Sweden*
[2]*Department of Materials Engineering, Universidade Tecnológica Federal do Paraná, CEP 86036-370, Londrina, PR, Brazil*
[3]*Department of Physics, Universidade Federal do Paraná, CP 19044, CEP 81531-990, Curitiba, Brazil*
[4]*Department of Physics, University of Oslo, P.O. Box 1048 Blindern, NO-0316 Oslo, Norway*

(Received 30 April 2012; published 29 July 2013)

Antiferromagnetic and ferromagnetic configurations of hematite α-Fe_2O_3 structures have been investigated by first-principles methods, which have been used to theoretically analyze the local structural and magnetic effects due to the presence of interstitial atoms such as hydrogen and oxygen. This study is based on the projector-augmented wave method within the local spin density approximation (LSDA) in addition to an on-site Coulomb correction of the Fe d orbitals (i.e., the LSDA + U^{SIC} method). The results demonstrate that this correction potential is important in achieving an accurate description of both the structural and the magnetic properties of α-Fe_2O_3. The ground state of α-Fe_2O_3 is the antiferromagnetic phase. The presence of oxygen vacancies, interstitial oxygen, and an interstitial hydrogen decreases the local Fe magnetic moment $|M_s(\mathrm{Fe})|$ in both the ferro- and antiferromagnetic phases, although the hydrogen has a rather modest effect. The density of states calculations demonstrate that the presence of interstitial atoms and defects yields a small reduction in the material's electronic gap.

DOI: 10.1103/PhysRevB.88.045136 PACS number(s): 71.20.Be, 71.55.Ak, 75.50.−y, 71.15.Mb

I. INTRODUCTION

The hematite α-Fe_2O_3 compound[1,2] is one of the most common iron oxides and is an important resource for the steel and electronics industry. The material has intriguing characteristics and has therefore been suggested for use in many types of technologies, such as magnetic and electronic devices,[3] sensor devices,[4,5] batteries,[6] hydrogen production,[7] photoelectrochemical applications,[8,9] and nanotechnology applications.[10–12] This broad range of applications has motivated investigations to understand the fundamental material properties.[13,14] At ambient conditions, hematite crystallizes in the rhombohedral $R\bar{3}c$ structure. The oxide exhibits an antiferromagnetic (AFM) behavior below $T_c = 955$ K (Ref. 15) but is weakly ferromagnetic (FM) at room temperature.[16] The material normally exhibits n-type semiconductor characteristics with a band gap of 1.6–2.2 eV.[14,17–19] However, the presence of interstitial atoms or vacancies can modify the electronic and optical properties and its semiconductor characteristics to p type. Some experimental works, such as Santilli *et al.*,[20] have suggested that the α-Fe_2O_3 p-type conductivity is only possible because of the presence of impurities. This proposal indicates that this material is affected by its stoichiometry, which is strongly dependent on its growth conditions. This phenomenon has been demonstrated, for instance, through scanning tunneling microscopy and low energy diffraction studies,[21] which also proved that structures such as FeO(111) can coexist with α-Fe_2O_3(0001). A theoretical study of α-Fe_2O_3 by Rollmann *et al.*[22] revealed a crystalline structure consistent with the experimental results,[23,24] and the calculations demonstrated that the insulating characteristic of this material is strongly dependent on the unit-cell volume due to a strong interaction between the Fe 3d and O 2p orbitals.

In this work, a first-principles theoretical study of AFM and FM configurations of bulk intrinsic α-Fe_2O_3 and compounds with high concentrations of native defects such as oxygen vacancies, oxygen interstitials, and hydrogen interstitials is presented. The crystalline structure, the atomic-resolved density-of-states (DOS) and magnetic properties of these structures are presented. To study these materials, the local spin density approximation (LSDA) with the on-site Coulomb correction of the Fe d orbitals according to the LSDA + U^{SIC} method was employed. Early LSDA studies[25,26] of intrinsic α-Fe_2O_3 in the AFM ground state revealed energy gaps in the electron DOS of each spin channel while providing evidence of a zero-gap compound for the total spin-independent DOS. A recent calculation[22] based on the gradient corrections in the exchange-correlation functional in combination with a Coulomb correction increased the energy gaps and improved the local magnetic moment. In general, the calculations presented here agree with the earlier calculations. The intrinsic α-Fe_2O_3 is also demonstrated to become an AFM insulator when the LSDA + U^{SIC} method is considered. This result is explained by the better localization of the lower Fe d states in the LSDA + U^{SIC} approach. Compared with the regular LSDA calculations, the localization of the d state LSDA + U^{SIC} implies a slightly small unit-cell volume and a 25% increased local magnetic field for the most stable AFM phase, which is important to consider when investigating the native defects in the compound. Using the LSDA + U^{SIC} approach, the oxygen vacancies were observed to have a local effect on the DOS due to the electron doping; the oxygen and hydrogen interstitials influence the band gap of the AFM structures.

II. COMPUTATIONAL METHOD

The ground-state crystalline phase of the α-Fe_2O_3 compound is the rhombohedral crystalline structure $R\bar{3}c$ (space group no. 167), which can also be described using a hexagonal coordinate system. In this work, the hexagonal structure with six (Fe_2O_3) formula units was selected, thus implying 30 atoms per unit cell (Fig. 1). The crystal is defined by positioning a Fe atom at the Wyckoff 12c sites with the principal coordinates

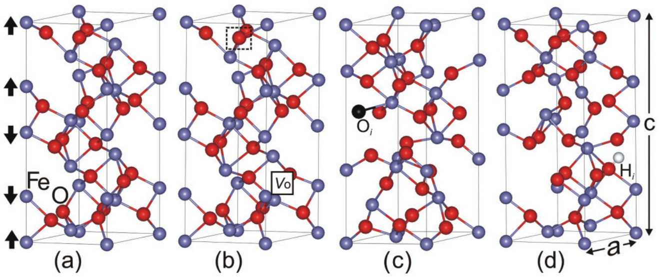

FIG. 1. (Color online) Relaxed crystalline structures of hematite α-Fe_2O_3 in the hexagonal coordinate system. (a) Intrinsic α-Fe_2O_3, where the arrows indicate the spin configuration of the AFM-II phase. The considered native defects are (b) oxygen vacancy V_O, (c) oxygen interstitial O_i (black atom), and (d) hydrogen interstitial H_i (gray atom). The additional dashed box in (b) indicates the position of the second V_O.

$(x, y, z) = (0, 0, z(\mathrm{Fe}) \approx 1/3)$ and an O atom at the Wyckoff 18*e* sites with $(x, y, z) = (x(\mathrm{O}) \approx 1/3, 0,1/4)$ in units of the hexagonal lattice vectors.

The compounds were analyzed using a projector-augmented wave method and the Kohn-Sham single-electron equation within the density functional theory (DFT).[27,28] To correct the LSDA exchange-correlation interaction, the LSDA + U^{SIC} method with an rotationally invariant self-interaction-like correction Coulomb potential was selected.[29] This on-site orbital-dependent correction potential is spatially more localized and more anisotropic, which is important for better describing *d* states.[30] In accordance with Refs. 22,31, and 32, an effective Coulomb $U_d = U - J = 4$ eV on the Fe *d* orbitals was employed. To analyze the effect of the localization effect of the Fe *d* states, a comparison between the LSDA + U^{SIC} results and the corresponding LSDA calculations was performed.

The effective interaction potentials within the LSDA and the LSDA + U^{SIC} approaches are obtained self-consistently with the energy cut-off of 400 eV. The cell volume and atom positions were optimized using a sequential approach, where the lattice constants were relaxed to a total energy accuracy of 0.001 eV and the atom positions were relaxed using the quasi-Newton algorithm of forces to an accuracy of 0.01 eV/Å on each atom. The total energy E_t, the atomic-resolved, spin-dependent DOS, and the local magnetic moments were obtained using the Gaussian **k**-space integration, which involved a smearing of $\sigma = 0.05$ eV and an $18 \times 18 \times 14$ Monkhorst-Pack **k**-mesh that implies 1197 **k**-points in the irreducible part of the Brillouin zone. The muffin-tin radii were $R_{\mathrm{MT}} = 1.50$ Å and 0.82 Å for Fe and O, respectively.

The analyses of high concentrations of native defects in the α-Fe_2O_3 compounds were performed with the small cells (30 atoms) involving high spatial symmetry of the defect sublattices but also with supercells constructed with $3 \times 3 \times 1$ (270 atoms) cells. The **k**-meshes for the supercells were $3 \times 3 \times 3$. The formation energy of the native hydrogen interstitial was calculated from $\Delta H_f(\alpha\text{-}Fe_2O_3{:}H_i) = E_t(\alpha\text{-}Fe_2O_3{:}H_i) - E_t(\alpha\text{-}Fe_2O_3) - \mu(H_2)/2$ using the large supercells, where the chemical potential $\mu(H_2)$ was estimated using the energy calculation of the H_2 molecule; a corresponding model was used for the native oxygen defects and oxygen vacancies with the respective adjustments.

III. RESULTS

The crystalline structure of α-Fe_2O_3 is presented in Fig. 1. Within the $R\bar{3}c$ space group symmetry, each of the 12 equivalent iron atoms (Fe) has octahedral site symmetry with six surrounding oxygen atoms (O). An ideal structure can thus have six equivalent Fe–O bonds; however, in the true α-Fe_2O_3 structure, there are two types of Fe–O bonds: three bonds with short bond lengths $\delta(\mathrm{Fe{-}O}^{(1)}) \approx 1.8$ Å and three with $\delta(\mathrm{Fe{-}O}^{(2)}) \approx 2.0$ Å. One can also characterize the local iron environment from the distance between the iron atoms, where $\mathrm{Fe}^{(1)}$ and the $\mathrm{Fe}^{(2)}$ represent the iron atoms along the *c* axis with the shortest and longest distances between them (Fig. 1). Each Fe has two neighboring Fe atoms with $\delta(\mathrm{Fe{-}Fe}^{(1)}) \approx 2.8$ Å and four neighboring Fe atoms with $\delta(\mathrm{Fe{-}Fe}^{(2)}) \approx 3.9$ Å.

While the FM phase is trivial, the AFM phase of α-Fe_2O_3 can exist in three different magnetic configurations. These magnetic configurations for the AFM phases lower the crystalline symmetry. The AFM-I phase has alternated spin-up and spin-down layers along the hexagonal *c* axis. The AFM-II phase [shown in Fig. 1(a)] has opposite spins between the shortest Fe–Fe distances along the hexagonal *c* axis and the same spin orientation between the longest Fe–Fe distances. Finally, the AFM-III phase has opposite spins between the longest Fe–Fe distances along the hexagonal *c* axis and the same spin orientation between the shortest Fe–Fe distances. The positions of the native defects (discussed in Secs. III B–III D) are also indicated in Figs. 1(b), 1(c), and 1(d).

A. Intrinsic α-Fe_2O_3

The optimization of the intrinsic α-Fe_2O_3 with the four different magnetic configurations (Table I) demonstrates that all the phases have a rather similar cell volume. As expected, due to the differences in their electronic configuration, all the AFM structures described a cell volume that was slightly smaller than the FM structure. Moreover, the space group symmetry is lowered in the AFM phases by the magnetic configuration. The AFM-II phase with opposite spins of Fe atoms with short bonds is the most stable structure, and this phase also has the smallest cell volume. The volume of the FM phase is comparable to that of the AFM-III phase with a larger lattice constant *a* and a small cell height (defined by *c*) compared with the other two AFM phases. The AFM-II phase is the most stable magnetic configuration while also having the smallest volume. These calculations are in very good agreement with the experimental crystalline structure,[33] although the theoretical lattice constant is underestimated, which is a normal effect in both LSDA and LSDA + U^{SIC}. The ionic positions and bonds are very similar. The principal coordinates (x, y, z) are (0, 0, 0.353) for the 12*c* Fe site and (0.305, 0, 1/4) for the 8*e* O site; these coordinates are (0, 0, 0.354) and (0.306, 0, 1/4) for the AFM-II phase. The FM configuration tends to generate shorter interatomic distances between the iron atoms, with $\delta(\mathrm{Fe{-}Fe}^{(1)}) \approx 2.76$ Å and $\delta(\mathrm{Fe{-}Fe}^{(2)}) \approx 3.90$ Å. The corresponding distances for

TABLE I. Structural and magnetic properties of intrinsic α-Fe$_2$O$_3$ obtained from the LSDA + U^{SIC} calculations with a several-step optimization scheme of the lattice parameters (a, c, and $V_0 = a^2c\sqrt{3}/2$) and the atom positions [z(Fe) and x(O)] within the space group of $R\bar{3}c$. The total energy difference ΔE_t from the AFM-II phase is the most stable ground-state configuration with a zero total magnetic moment M_s and a local magnetic moment of $|M_s(\mathrm{Fe})| = 4.04\ \mu_{\mathrm{B}}$/Fe. The average bond lengths from Fe to neighboring O atoms δ(Fe–O) and neighboring Fe atoms δ(Fe–Fe) are fairly similar for all four magnetic phases.

α-Fe$_2$O$_3$	FM	AFM-I	AFM-II	AFM-III	Expt. AFM
a [Å]	5.01	4.96	4.92	4.98	5.03[a]
c/a	2.66	2.71	2.73	2.69	2.73[a]
V_0 [Å^3]	290.8	286.4	283.1	287.3	301.8[a]
z(Fe)	0.353	0.352	0.354	0.353	
x(O)	0.305	0.308	0.306	0.301	
δ(Fe–O$^{(1)}$) [Å]	1.93	1.89	1.91	1.92	1.99[a]
δ(Fe–O$^{(2)}$) [Å]	2.06	2.11	2.06	2.07	2.06[a]
δ(Fe–Fe$^{(1)}$) [Å]	2.76	2.82	2.81	2.78	2.88[a]
δ(Fe–Fe$^{(2)}$) [Å]	3.90	3.90	3.92	3.91	3.98[a]
M_s [μ_{B}/cell]	58.63	0.00	0.00	0.00	
$\lvert M_s(\mathrm{Fe})\rvert$ [μ_{B}/Fe]	4.28	4.13	4.04	4.16	4.64[b]
ΔE_t [eV/cell]	4.54	2.07	0	2.66	

[a] Reference 13.

[b] Reference 38.

the AFM-I and AFM-II configurations are $\delta(\mathrm{Fe–Fe}^{(1)}) \approx 2.81$ Å and $\delta(\mathrm{Fe–Fe}^{(2)}) \approx 3.91$ Å; thus, the AFM phases have somewhat more equal distances between the magnetic Fe atoms. AFM-II has $\delta(\mathrm{Fe–Fe}^{(1)})$ bond lengths that are between those of FM and AFM-II.

From the total energy calculations, the AFM-II phase was observed to have the most stable ground state. The energy differences between the AFM-II phase and the FM and other two AFM phases are significant, although the local magnetic moments of the Fe atoms are comparable ($|M_s(\mathrm{Fe})| = 4.04 - 4.28\ \mu_{\mathrm{B}}$/Fe). This finding is consistent with earlier theoretical results (Refs. 22,26, and 34), and the measurements indicate a magnetic moment of 4.64 μ_{B}/Fe (Ref. 38). Moreover, the measurements demonstrate AFM behavior below 955 K (Ref. 15). The total magnetization M_s for FM is mainly from the Fe sites (88%), with 12% being from the interstitial and induced magnetization of the surrounding oxygen atoms.

The total DOS of the four phases (Fig. 2) predicts that the FM phase has a zero energy gap. AFM-I, AFM-II, and the AFM-III phases have an energy gap of 0.8, 1.3, and 0.6, respectively. Even using similar calculations parameters, this energy gap is not observed in the DOS from the regular LSDA calculation [Fig. 3(c)]. With the LSDA + U^{SIC} correction, the calculated energy gap agrees better with the measured values of 1.6–2.2 eV,[14,17–19] although these values are underestimated, as expected.

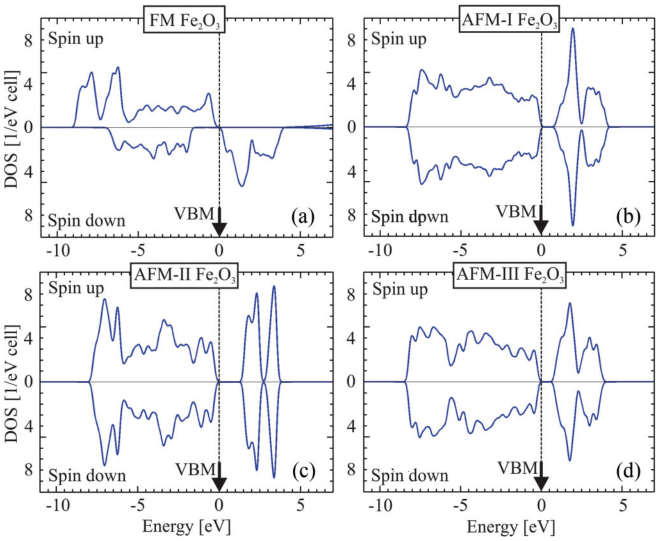

FIG. 2. (Color online) Spin-dependent total DOS of (a) FM, (b) AFM-I, (c) AFM-II, and (d) AFM-III using the LSDA + U^{SIC} method, presented with a 0.1-eV Lorentzian broadening. The energy refers to the highest populated electron state (indicated by a vertical dashed line). From the total energy (Table I), AFM-II is the most stable ground-state configuration.

Although different calculation methods (Table II) reveal overall fairly similar results, and all of these methods predict AFM-II as a stable phase, noticeable differences are apparent between certain methods. For instance, regular LSDA yields much stronger AFM-II stability and a smaller cell volume compared with LSDA + U^{SIC} and the hybrid functional Becke, 3-parameter, Lee-Yang-Parr (B3LYP). In addition, the local magnetization appears to be strongly underestimated in the LSDA: 3.18 μ_{B}/Fe compared with 4.28 μ_{B}/Fe for LSDA + U^{SIC} and 4.27 μ_{B}/Fe for B3LYP. This result was

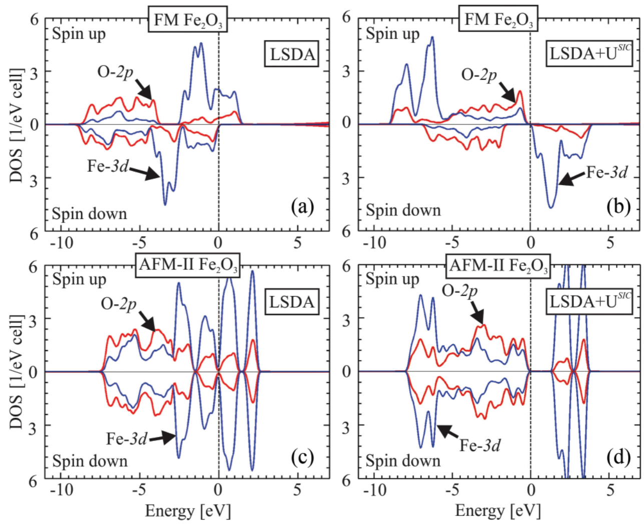

FIG. 3. (Color online) Angular-resolved and spin-dependent DOS of FM α-Fe$_2$O$_3$ from the (a) LSDA and (b) LSDA + U^{SIC} calculations and the corresponding DOS of AFM-II α-Fe$_2$O$_3$ from (c) LSDA and (d) LSDA + U^{SIC}, presented with a 0.1-eV Lorentzian broadening. Fe 3d and O 2p are represented by the blue and red lines, respectively. The energies refer to the highest populated electron state. The LSDA + U^{SIC} method clearly energetically localizes the lower Fe 3d states (resulting in a narrower valence band), which also directly affects the O states. One can observe that LSDA yields a nearly zero energy gap, whereas the LSDA + U^{SIC} method generates a phase with an overall and spin-independent insulator property for the AFM-II phase.

TABLE II. Comparison of our LSDA and LSDA + U^{SIC} calculations with earlier published theoretical results (see Refs. 22,26, and 34). See Table I for definition of the parameters. One can notice the difference between LSDA and the other methods, especially for the FM phase.

	This work				Ref. 26		Ref. 22		Ref. 34	
	LSDA + U		LSDA		LSDA		GGA[a]		B3LYP[b]	
α-Fe_2O_3	FM	AFM-II	FM	AFM-II	FM	AFM-II	FM	AFM-II	FM	AFM-II
a [Å]	5.01	4.92	4.91	4.90			4.77	5.00	5.13	5.08
c/a	2.66	2.73	2.78	2.80			2.80	2.77	2.72	2.74
V_0 [Å^3]	290.8	283.1	285.0	286.8			263.7	300.0	318.0	311.1
$\lvert M_s(\mathrm{Fe})\rvert$ [μ_B/Fe]	4.28	4.04	3.18	3.00	3.73	3.72	2.6	3.44	4.27	4.16
ΔE_t [eV/cell]	4.54	0	7.50	0	5.8	0	4.66	0	3.28	0

[a] Generalized gradient approximation.

[b] B3LYP is a hybrid functional.

also observed by Rollmann *et al.*[22] Moreover, by comparing the DOS results (Fig. 3) from the LDA calculations with the LSDA + U^{SIC} calculations, one observes that the latter calculations generate broader valence DOS for both FM and AFM-II with more localized Fe 3d energy states. Whereas LSDA yields a metallic FM phase, LSDA + U^{SIC} generates an electronic structure with states at the Fermi energy. Moreover, the angular-dependent potential within LSDA + U^{SIC} increases the energy gap for the AFM-II phase from approximately 0 eV to 1.3 eV. This result is much more consistent with the measured gap energy of 1.6–2.2.[14,17–19] Thus, the results demonstrate that the correction potential within LSDA + U^{SIC} is important for achieving accurate structural, electronic, and magnetic properties of α-Fe_2O_3.

B. Oxygen vacancy

One may expect that defects close to Fe will change the population of Fe 3d states and thereby affect the local magnetization around the atom. With a sufficient number of defects, the magnetic phase will also be affected. Because the symmetry of the crystal is lowered by the defects, the configuration of the lowest ground state may also change. That is, defect-rich α-Fe_2O_3 may exhibit FM ground-state properties in contrast to the intrinsic α-Fe_2O_3 with AFM-II phase. Likewise, as discussed in earlier studies, a high concentration of oxygen vacancies can lead to important changes in the electronic structures of this material.[20,35] In this work, this hypothesis is investigated by adding one oxygen vacancy (V_O) in the 30 atom unit cell [see Fig. 1(b)]. A second vacancy (indicated by the dashed box in the figure) positioned far away from first vacancy was also included. The presence of V_O directly changes the Fe-Fe$^{(1)}$ and Fe-Fe$^{(2)}$ distances next to the vacancy (Table III). These structural changes resulted in a reduction of the local magnetic moment. Oxygen vacancies act as donorlike defects that directly decrease the total magnetization for the Fe-based α-Fe_2O_3. However, the effect is weak because the main change in charges occurs near the V_O site, producing more delocalized defect states. For the FM phase, the total magnetic moment decreases from 58.63 μ_B/cell for defect-free α-Fe_2O_3 to 56.44 and 54.61 μ_B/cell for α-Fe_2O_3:V_O and α-Fe_2O_3:2V_O, respectively. Considering that each V_O is surrounded by four Fe atoms, the analyses of the local effect on their magnetic moment reveals that the two Fe atoms with the largest distance δ(Fe–O$^{(2)}$) undergo a reduction of 10% in their magnetic moments. However, the remaining Fe atoms with the shortest distance δ(Fe–O$^{(1)}$) exhibited a reduction of 3%. This result is expected because the oxygen removed to produce the vacancy leads to an electronic charge increase on these Fe atoms. The

TABLE III. Structural and magnetic properties of defect-rich α-Fe_2O_3 for the FM and AFM-II phases. The bond lengths describe the bonds next to the defect.

	a [Å]	c/a	$\lvert M_s(\mathrm{Fe})\rvert$ [μ_B/Fe]	δ(Fe–O$^{(1)}$) [Å]	δ(Fe–O$^{(2)}$) [Å]	δ(Fe–Fe$^{(1)}$) [Å]	δ(Fe–Fe$^{(2)}$) [Å]
				FM phase			
α-Fe_2O_3	5.01	2.66	4.28	1.93	2.06	2.76	3.91
α-Fe_2O_3:V_O	5.00	2.69	4.25	1.91	2.06	2.88	3.95
α-Fe_2O_3:2V_O	4.97	2.73	4.13	1.91	2.06	2.86	3.97
α-Fe_2O_3:O$_i$	5.07	2.61	4.08	1.96	2.08	2.78	3.83
α-Fe_2O_3:H$_i$	4.96	2.73	4.28	1.92	2.07	2.74	4.17
				AFM-II phase			
α-Fe_2O_3	4.92	2.73	4.04	1.91	2.06	2.81	3.92
α-Fe_2O_3:V_O	4.92	2.74	3.95	1.88	2.05	2.90	3.87
α-Fe_2O_3:2V_O	4.92	2.73	3.95	1.88	2.06	2.89	3.89
α-Fe_2O_3:O$_i$	4.98	2.71	4.02	1.90	2.10	2.79	4.10
α-Fe_2O_3:H$_i$	4.92	2.75	4.01	1.90	2.08	2.77	4.16

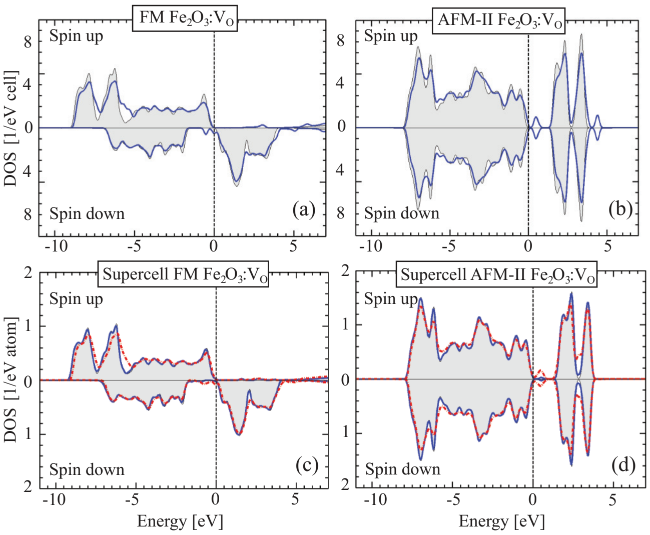

FIG. 4. (Color online) Spin-dependent total DOS of the (a) FM and (b) AFM-II phases of α-Fe_2O_3 with one oxygen vacancy V_O (blue, thick line) in the $1 \times 1 \times 1$ crystal cells. This figure demonstrates that the oxygen vacancy only has a minor effect on the DOS. The corresponding DOS of the (c) FM and (d) AFM-II phases in the nine-times-larger cell (i.e., a $3 \times 3 \times 1$ supercell) with low-defect density (blue line) and high-defect density (dashed red line) of oxygen vacancies demonstrates that this defect configuration only has a modest effect on the local DOS using a well-located or randomly distributed configuration. The DOS is presented in units of 1/(eV·atom) to scale the DOS using the number of defects. For comparison, the DOS for intrinsic α-Fe_2O_3 (gray areas) is also presented, and all the results are presented with a 0.1-eV Lorentzian broadening. The data is from the LSDA + $U^{\rm SIC}$ calculations, and the energies refer to the highest populated electron state.

TABLE IV. The magnetization and the formation energies ΔH_f of native defects in α-Fe_2O_3 obtained from the LSDA + $U^{\rm SIC}$ calculations with the $3 \times 3 \times 1$ supercell (270 atoms for the defect-free cell). We present results for low-defect density (one defect per cell) and high-defect density (nine defects per cell). The values in brackets indicate the formation energy per defect.

	$\lvert M_s(\mathrm{Fe})\rvert$ $[\mu_B/\mathrm{Fe}]$		ΔH_f [eV]	
Defects	FM	AFM-II	FM	AFM-II
α-Fe_2O_3:V_O	4.03	4.03	4.25	4.39
α-Fe_2O_3:9V_O	4.19	3.97	32.25	40.33
			(3.58)	(4.48)
α-Fe_2O_3:O_i	4.26	4.03	2.50	2.52
α-Fe_2O_3:9O_i	4.06	4.03	12.98	39.04
			(1.42)	(4.33)
α-Fe_2O_3:H_i	4.27	4.03	−0.02	0.66
α-Fe_2O_3:9H_i	4.05	4.08	−1.95	14.32
			(−0.21)	(1.59)

DOS of the FM phase has a modest effect on the electronic structure due to the presence of V_O (Fig. 4). In the AMF-II phase, however, the defect states appear in the band-gap region and will thereby diminish the insulating properties. We also investigated the effects due to the configuration of the defects. The DOS for α-Fe_2O_3:V_O in the small crystal cell (thus, the defect sublattice has high spatial symmetry) is compared with the corresponding α-Fe_2O_3:V_O DOS in the nine-times-larger supercell with a more random distribution of the nine V_O (Fig. 4). Only a small difference in the DOS exists between these two vacancy configurations, where, as expected, the random distribution exhibits a mitigation of the DOS of the FM and AFM-II phases. In Figs. 4(c) and 4(d), one can compare the effect of the DOS dispersion for an increased concentration of defects. The compound with a high density of oxygen vacancies (i.e., nine randomly distributed V_O in the supercell; red dashed line) exhibits a somewhat broader DOS compared with the corresponding compound with a low density of vacancies (i.e., one V_O in the supercell; blue line). However, the broadening effect is moderate. Moreover, the random distribution of vacancies is well mimicked by the small cell structure with the same density of vacancies.

A special interest is the possibility of converting an AFM α-Fe_2O_3 structure to a FM structure due to the high density of defects. However, a magnetic phase modification was not observed, even with the presence of two oxygen vacancies. The total energy difference (e.g., Table I) is $\Delta E_t \approx 3.8$ eV for α-Fe_2O_3:V_O and $\Delta E_t \approx 3.3$ eV for α-Fe_2O_3:2V_O. These values are smaller than the corresponding energy for defect-free α-Fe_2O_3 but demonstrate that the AFM-II configuration is still the most stable structure even in the oxygen-deficient α-Fe_2O_3 materials. Hence, a strong reconstruction to a high-symmetry phase is required to achieve the magnetic transition to the FM phase.

The defect formation energies of V_O in the FM and AMF-II phases are calculated using the 270-atom supercells to simulate low and high concentrations of defects. The V_O formation energies for the most stable phases AFM-II ($\Delta H_f = 4.39$ eV) and the FM phase ($\Delta H_f = 4.25$ eV) are rather similar, indicating that the magnetic configuration has less of an effect on the oxygen defects. Approximately 4 eV was required to remove one or several oxygen atoms in the material (Table IV). The fact that this energy cost does not increase significantly with respect to already present vacancies is an indication that oxygen-poor iron oxide phases can be formed. Although the FM phase is expected to be more significantly affected by the defects, the magnetization for a high concentration of randomly distributed defects has a major effect on both phases.

C. Oxygen interstitial

Oxygen is also known to occupy an interstitial site. From the 270-atom supercells, the defect formation energies of oxygen on an interstitial site (O_i) in the FM and AFM-II phase are 2.50 and 2.52 eV, respectively (Table IV). With high concentrations of O_i, one can expect a significant impact on the crystal structure and magnetic properties. By adding O_i in the hematite cell [see Fig. 1(c)], where the O_i is represented by the black atom, we observe that the oxygen interstitial in the cell affects the local magnetization. The crystal symmetry is affected by the interstitial atom, which promotes a reorganization of the iron atoms with an increase in the cell volume (Table III). This process also results in a reduction in its magnetization. For the nine-times-larger cell, this effect is clarified for a low density of oxygen interstitials (one O_i per supercell), where the FM

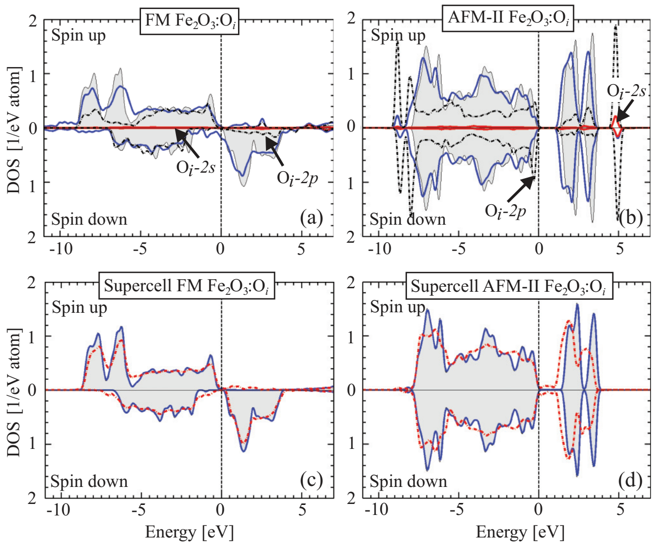

FIG. 5. (Color online) Spin-dependent total DOS of (a) FM and (b) AFM-II α-Fe$_2$O$_3$ with one interstitial O$_i$ in the $1 \times 1 \times 1$ crystal cells. The thin (blue) lines represent α-Fe$_2$O$_3$:O$_i$, and the thick (red) lines and dashed lines indicate the partial DOS of the sole O$_i$ atom. The DOS is presented in units of 1/(eV·atom) to illustrate the DOS for the sole interstitial atom. (c) FM and (d) AFM-II DOS of the α-Fe$_2$O$_3$ nine-times-larger cell (i.e., a $3 \times 3 \times 1$ supercell), with one (blue line) and nine (dashed red line) interstitial O$_i$. In contrast to the oxygen vacancy (Fig. 4), the interstitial oxygen reduces the material energy gap in the well-located interstitial atom structure and in the randomly distributed structure. The gray areas represent the DOS of the intrinsic α-Fe$_2$O$_3$ material, and all the results are presented with a 0.1-eV Lorentzian broadening.

phase magnetization is modestly affected. However, a major effect on the magnetization is observed when nine oxygen atoms are randomly distributed at the supercell interstitials, nine Oi per supercell (Table IV).

With respect to the electronic structure of the α-Fe$_2$O$_3$, the addition of one oxygen atom may be an important tool to tailor its electronic gap.[31] Figures 5(a) and 5(b) present the DOS of FM and AFM-II structures with an O$_i$ in the small crystal cell scaled to 1/(eV·atom). Comparable to the oxygen vacancies, the oxygen interstitials have a minor effect on the overall electronic structure. However, the O$_i$ $2p$ states in AFM-II are form-defect states energetically above the valence-band maximum. Thus, the effect of the $2p$ orbital from the O$_i$ atom on the AFM structure promotes a small reduction in the electronic gap, and an increase in the states near the zero energy is also observed at the DOS from the FM structure. Thus, the calculations demonstrate the possibility to control, to some extent, the band-gap energy without forming defect states in the gap region. Because the topmost valence states are O$_i$ $2p$-like, these spatially localized states imply an inhomogeneity of the electronic dispersion in the material.

The total energy difference between the AFM-II and FM phases of α-Fe$_2$O$_3$:O$_i$ indicates whether the defect destabilizes the AFM-II phase. For the $3 \times 3 \times 1$ supercell, this energy difference is 5.1 eV. For α-Fe$_2$O$_3$:O$_i$ the energy difference is the same. Thus, low concentration of oxygen interstitial atoms does not destabilize the AFM-II phase. However, for high concentrations, the material becomes more paramagnetic. For instance, with nine oxygen atoms in the $3 \times 3 \times 1$ cell (i.e., α-Fe$_2$O$_3$:9O$_i$), the corresponding energy difference is only 2.1 eV, though the magnetic moment is only slightly decreased. The AFM-II phase presents higher defect-formation energy than in the FM phase, and the addition of more atoms intensified this behavior (Table IV). This indicates, in combination with the total energy difference of the phases, a higher stability of the AFM phase even when interstitial oxygen atoms are added. A comparison of the DOS for the nine-times-larger cell with a low and high density of defects, illustrated in Figs. 5(c) and 5(d), corroborates the above statement. The effect on the DOS by increasing the interstitial oxygen number is followed by gap reduction due to the new electronic charges on the system.

D. Hydrogen interstitial

Hydrogen is always present in iron oxide steel-processing technologies. Depending on the chemical potential, the interstitial hydrogen (H$_i$) can act as an electronic acceptor or donor in the material.[36–38] In this work, H$_i$ was added at an interstitial site of the unit cell [see Fig. 1(d)], where the gray atom indicates the position of the H$_i$. The addition of the hydrogen atom may result in a smaller effect on the local magnetization compared with O$_i$ due to its different electron affinity and valence configuration. This result is

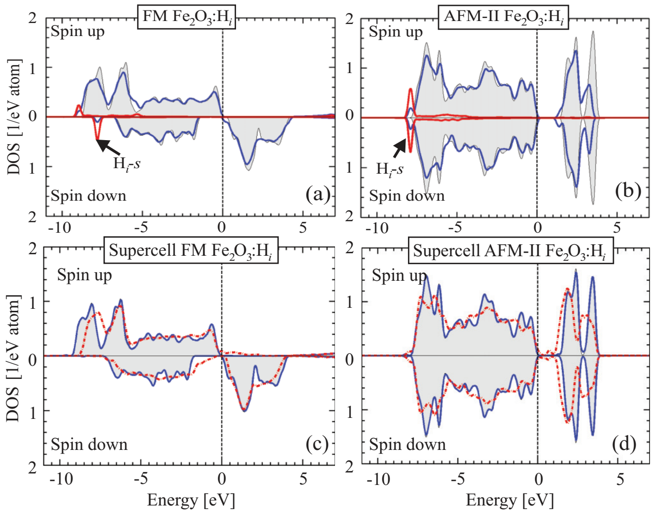

FIG. 6. (Color online) Spin-dependent total DOS of (a) FM and (b) AFM-II α-Fe$_2$O$_3$ with one interstitial H$_i$ in the $1 \times 1 \times 1$ crystal cells. The thin (blue) lines represent α-Fe$_2$O$_3$:H$_i$, and the thick (red) lines indicate the partial DOS of the sole H atom. The DOS is presented in units of 1/(eV·atom) to illustrate the DOS for the sole interstitial atom. The corresponding DOS for (c) FM and (d) AFM-II α-Fe$_2$O$_3$ are presented for one (blue line) and nine (dashed red line) interstitials H$_i$ in the nine-times-larger cell $3 \times 3 \times 1$ supercell. Similar to the oxygen interstitial (Fig. 5), the presence of well-located or randomly distributed interstitial hydrogen reduces the α-Fe$_2$O$_3$ energy gap. The gray areas represent the DOS of the intrinsic α-Fe$_2$O$_3$ material, and all the results are presented with a 0.1-eV Lorentzian broadening.

directly observed in the total energy difference between the FM and AFM-II phases. Whereas oxygen interstitials strongly stabilize the AFM-II phase, hydrogen interstitials somewhat destabilize the AFM-II phase: $\Delta E_t \approx 3.9$ eV for α-Fe_2O_3:H_i. Moreover, the defect formation energies of H_i are -0.02 and 0.66 eV for the FM and AFM-II phases, respectively, and the same behavior is observed for the structure with a high density of interstitial hydrogen atoms (Table IV). The negative value (though $\approx$0 eV) of the defect-formation energy for interstitial hydrogen atoms is due to approximations of the chemical potential, neglecting temperature and pressure dependences. However, the nearly zero formation energy of H_i indicates that hydrogen, as expected, will be easily accommodated in α-Fe_2O_3. Moreover, it is evident from Table III that the overall crystal structure is less affected by the interstitial hydrogen as compared with corresponding oxygen incorporation. In addition, the local magnetization of the Fe is not affected by H_i, whereas O_i decreases the magnetization in the FM phase. The same behavior is observed for the $3 \times 3 \times 1$ supercells with a low density (one H_i per supercell) and high density (nine H_i per supercell), as presented in Table IV.

Figure 6 presents the DOS of the FM and AFM-II structures with the H_i addition. The topmost valence-band region is nearly unaffected by hydrogen. The H_i $1s$ states are localized in the lower part of the valence band. However, the H_i defects form defect unpopulated states energetically just below the host conduction-band minimum for both the FM and AFM-II phases. The DOS for α-Fe_2O_3:H_i with a random distribution of nine H_i, shown in Figs. 6(c) and 6(d), demonstrates a similar effect as on the well-located interstitial hydrogen but with some mitigation of the presented states.

IV. SUMMARY

To summarize, our DFT/LSDA + U^{SIC} studies of intrinsic and defect-rich hematite α-Fe_2O_3 demonstrate that the on-site Coulomb correction of the Fe d is important in achieving an accurate description of the structural, electronic, and magnetic properties of α-Fe_2O_3. Significant changes were observed in the ground-state energy and magnetization around the defects with a strong correlation with Hund's rules. The most stable ground-state phase is the α-Fe_2O_3 AFM structure with opposite spins between the shortest Fe–Fe distances along the hexagonal c axis and the same spin orientation between the longest Fe–Fe distances. This structure was in good agreement with the experimental lattice constant, iron magnetization, and an expected underestimated electronic gap. The presence of native defects (vacancies, interstitial oxygen, and interstitial hydrogen) in the α-Fe_2O_3 structures changes the bond between Fe–O and Fe–Fe close to the defects, implying a reduction of its electronic gap and local iron magnetization. This material behavior is also observed for the supercell structure with a more random defect distribution. The interstitial oxygen strongly stabilizes the AFM phase while simultaneously decreasing the band-gap energy without forming defect states in the band-gap region.

ACKNOWLEDGMENTS

The authors acknowledge financial support from the European EM-ECW Program EUBRANEX, the Swedish Energy Agency, the Swedish Research Council, and the Brazilian agencies CNPq and CAPES-REUNI. We also acknowledge the access provided to supercomputer resources at NSC and HPC2N through SNIC/SNAC.

---

[1] L. Machala, R. Zboril, and A. Gedanken, J. Phys. Chem. B **111**, 4003 (2007).

[2] M. Catti, G. Valerio, and R. Dovesi, Phys. Rev. B **51**, 7441 (1995).

[3] S. Bae, S. Zurn, W. F. Egelhoff, Jr., P. J. Chen, L. Sheppard, E. J. Torok, and J. H. Judy, IEEE Trans. Magn. **37**, 3960 (2001).

[4] C. Wu, P. Yin, X. Zhu, C. OuYang, and Y. Xie, J. Phys. Chem. B **110**, 17806 (2006).

[5] S. Pal, E. B. Setterington, and E. C. Alocilja, IEEE Sens. J. **8**, 647 (2008).

[6] S. Zeng, K. Tang, T. Li, Z. Liang, D. Wang, Y. Wang, and W. Zhou, J. Phys. Chem. C **111**, 10217 (2007).

[7] M. A. Gondal, A. Hameed, Z. H. Yamani, and A. Suwaiyan, Appl. Catal. A **268**, 159 (2004).

[8] N. T. Hahn, H. Ye, D. W. Flaherty, A. J. Bard, and C. B. Mullins, Acs Nano **4**, 1977 (2010).

[9] T. Lopes, L. Andrade, H. A. Ribeiro, and A. Mendes, Int. J. Hydrogen Energy **35**, 11601 (2010).

[10] C. E. Cava, R. Possagno, M. C. Schnitzler, P. C. Roman, M. M. Oliveira, C. M. Lepiensky, A. J. G. Zarbin, and L. S. Roman, Chem. Phys. Lett. **444**, 304 (2007).

[11] F. Bødker, M. F. Hansen, C. B. Koch, K. Lefmann, and S. Mørup, Phys. Rev. B **61**, 6826 (2000).

[12] J. Chen, L. Xu, W. Li, and X. Gou, Adv. Mater. **17**, 582 (2005).

[13] L. Pauling and S. B. Hendricks, J. Am. Chem. Soc. **47**, 781 (1925).

[14] F. J. Morin, Phys. Rev. **93**, 1195 (1954).

[15] C. W. Searle and G. W. Dean, Phys. Rev. B **1**, 4337 (1970).

[16] N. Amin and S. Arajs, Phys. Rev. B **35**, 4810 (1987).

[17] S. Mochizuki, Phys. Status Solidi A **41**, 591 (1977).

[18] J. K. Leland and A. J. Bard, J. Phys. Chem. **91**, 5076 (1987).

[19] R. F. G. Gardner, F. Sweett, and D. W. Tanner, J. Phys. Chem. Solids **24**, 1183 (1963).

[20] C. V. Santilli, J. P. Bonnet, P. Dordor, M. Onillon, and P. Hagenmuller, Ceram. Int. **16**, 25 (1990).

[21] N. G. Condon, F. M. Leibsle, A. R. Lennie, P. W. Murray, D. J. Vaughan, and G. Thornton, Phys. Rev. Lett. **75**, 1961 (1995).

[22] G. Rollmann, A. Rohrbach, P. Entel, and J. Hafner, Phys. Rev. B **69**, 165107 (2004).

[23] G. K. Rozenberg, L. S. Dubrovinsky, M. P. Pasternak, O. Naaman, T. Le Bihan, and R. Ahuja, Phys. Rev. B **65**, 064112 (2002).

[24] J. Badro, G. Fiquet, V. V. Struzhkin, M. Somayazulu, H.-K. Mao, G. Shen, and T. Le Bihan, Phys. Rev. Lett. **89**, 205504 (2002).

[25] L. M. Sandratskii, M. Uhl, and J. Kübler, J. Phys.: Condens. Matter **8**, 983 (1996).

[26] L. M. Sandratskii and J. Kübler, Europhys. Lett. **33**, 447 (1996).

[27] G. Kresse and D. Joubert, Phys. Rev. B **59**, 1758 (1999).

[28] P. E. Blöchl, Phys. Rev. B **50**, 17953 (1994).

[29] A. I. Liechtenstein, V. I. Anisimov, and J. Zaanen, Phys. Rev. B **52**, R5467 (1995).

[30] P. Mohn, C. Persson, P. Blaha, K. Schwarz, P. Novák, and H. Eschrig, Phys. Rev. Lett. **87**, 196401 (2001).

[31] Z. D. Pozun and G. Henkelman, J. Phys. Chem. **134**, 224706 (2011).

[32] Samir F. Matar, Prog. Solid State Chem. **31**, 239 (2003).

[33] P. Villars, *Pearson's Handbook: Crystallographic Data for Intermetallic Phases*, *Desk Ed.* (ASM International, Materials Park, Ohio, 1997).

[34] N. C. Wilson and S. P. Russo, Phys. Rev. B **79**, 094113 (2009).

[35] Z. Chen, U. Cvelbar, M. Mozetič, J. He, and M. K. Sunkara, Chem. Mater. **20**, 3224 (2008).

[36] C. G. Van de Walle and J. Neugebauer, Nature **423**, 626 (2003).

[37] V. V. Kriventsov and D. I. Kochubey, J. Mol. Catal. A: Chem. **158**, 287 (2000).

[38] J. M. D. Coey and G. A. Sawatzky, J. Phys. C **4**, 2386 (1971).